The final version of this research article was published by the AIAA Journal. https://doi.org/10.2514/1.J058148

Influence of Wake and Background Turbulence on Predicted Fan Broadband Noise

Carolin A. Kissner [a] and Sébastien Guérin [b]
German Aerospace Center (DLR), Berlin, Germany

Next generation fan designs featuring large bypass ratios have the potential to reduce rotor-stator-interaction noise of fans. However, these designs pose new challenges and long-held beliefs regarding the acoustic benefit of such concepts need to be evaluated. At off-design operating points, the increase in nozzle area serves to maintain the stall margin by reducing the fan loading. To an extent, this may lower the contribution of wake turbulence to fan broadband noise. Thus, investigating the relative contribution of other noise sources becomes relevant. In this paper, the authors examine the contribution of wake and ingested turbulence to fan broadband noise levels at approach for the ASPIRE fan, which is a next generation fan concept. To enable the investigation of background turbulence, a Reynolds stress turbulence model is used. The CFD solution then provides inputs for a 2D cyclostationary synthetic turbulence method. The noise predictions are improved by performing simulations at three spanwise positions and by introducing a correction technique to account for the three-dimensional interstage flow. For the investigated case, it is shown that broadband noise generated at the stator is as high as for conventional concepts. Furthermore, both wake and background turbulence contribute significantly to the overall fan broadband noise.

[a] Research Engineer, German Aerospace Center (DLR), Institute of Propulsion Technology, Department of Engine Acoustics.

[b] Senior Research Scientist, German Aerospace Center (DLR), Institute of Propulsion Technology, Department of Engine Acoustics.

Nomenclature

B	=	number of rotor blades
H_t	=	total specific enthalpy, J/K
k_t	=	turbulent kinetic energy, m^2/s^2
L_W	=	sound power level, dB ref 10^{-12} W
P	=	sound power, W
S_{22}	=	upwash velocity frequency spectral density, m^2/s
U_{tip}	=	fan tip speed, m/s
β	=	rotor scaling factor
η_{isen}	=	fan isentropic efficiency
θ_w	=	wake width, rad
$\widetilde{\theta_w}$	=	non-dimensional wake width
Λ	=	integral turbulent length scale, m
Π	=	fan pressure ratio
ψ	=	rotor loading
ω_t	=	turbulent dissipation rate, s^{-1}

Sub- and Superscripts

b	=	background
C	=	circumferentially averaged, constant
P	=	spectrally averaged, periodic
w	=	wake

I. Introduction

To maximize the efficiency of aircraft engines, next generation turbofans will have larger-than-ever bypass ratios and will likely be equipped with so-called Variable Area Nozzles (VAN's) to ensure stable operating conditions at off-design. At off-design points such as take-off and approach, the nozzle area can be increased to maintain the stall margin. This results in a reduced loading of the rotor blades and thus a reduction in wake turbulence. While the use of VAN's may help to reduce both tonal and broadband rotor-stator-interaction noise, it can affect the relative contribution of

other noise sources that are oftentimes neglected in today's noise predictions. One potentially relevant broadband noise source is ingestion noise, which is produced by the interaction of ingested turbulence, i. e. background turbulence, with the rotor and stator leading edges. Many fan rigs and full-scale outdoor test beds feature a small, but not negligible level of background turbulence. Neglecting this effect can falsify the interpretation of experimental and numerical data, which can negatively impact the design process itself.

In order to study the contribution of background as well as wake turbulence to the overall fan broadband noise level, the authors studied a realistic next generation fan design and employed methods capable of considering background turbulence.

The ASPIRE fan concept, which was designed and optimized by Schnell et al. [1], aims at being representative for the next generation of civil aero-engines and assumes the use of 2025+ technology. Its engine bypass ratio of about 16 at the aerodynamic design point is significantly higher compared to today's modern engines. Furthermore, its design pressure ratio of 1.31 at cruise is closer to the expected maximum aerodynamic efficiency, which Moreau and Guérin [2] have estimated to be about 1.2. To counteract stability issues at takeoff - as discussed by Cumptsy [3] - but also at approach, the ASPIRE fan concept is equipped with a VAN. At approach conditions, the nozzle area is increased by about 4.2%. Yet, the rotor loading $\psi = 0.34$ (see definition in appendix) is still high compared to fans operating with higher fan pressure ratios. Nonetheless, the design avoids rotor-leading edge flow separations - as reported e. g. by Prasad and Prasad [4]. The authors assume that these features are typical for a next generation fan and makes this fan ideal for studying the potential influence of background turbulence.

Synthetic turbulence methods are promising for studying fan broadband noise as they are reasonably fast for performing parameter studies. Recent advances have included their expansion to three-dimensional space [5–8], to anisotropic turbulence [9], and to cyclostationary turbulence and flow [10, 11]. The capability of the fRPM-fan method to consider cyclostationarity is necessary for studying the relative contribution of background turbulence. It can reconstruct wake structures in terms of the mean flow and turbulence characteristics and thus consider broadband noise generated at the stator by both wake and background turbulence. Some changes were made to the process

chain of the fRPM-fan method to enable the correct realization of background turbulence and to address some shortcomings of the original 2D method. Firstly, a Reynolds stress turbulence model was applied as the authors found that the realization of the turbulent length scale between the wakes is compromised when applying a conventional two-equation turbulence model based on the Boussinesq hypothesis. Secondly, the parameter study conducted by Wohlbrandt et al. [10] was performed on one streamline at 50% of the stator height. While the agreement between numerical and experimental data was satisfactory for the NASA SDT fan at approach conditions, the question remained whether a midspan slice can be truly representative for the entire 3D duct. To reduce this uncertainty, simulations at three different streamline positions were performed in this paper. Thirdly, the operating conditions of the quasi-three-dimensional (q3D) URANS simulations at the different streamline positions were set by matching the incidence angle of the 3D RANS simulation. Because radial flow gradients are suppressed, the rotor wake structures of the q3D simulations oftentimes tend to differ from those of a 3D RANS simulation. A correction technique based on analysis of upwash velocity frequency spectra was introduced to account for this issue. Lastly, turbulence is synthesized at the location of the vortex source by reconstructing harmonics from the q3D URANS simulations. Since the vortex source cannot be located directly at the stator leading edge (LE), the wake development cannot be inherently considered by the cyclostationary fRPM-fan method. A correction technique based on the analysis of upwash velocity frequency spectra was introduced to account for differences in flow between q3D and 3D CFD simulations and to account for the wake development between the vortex source and the stator leading edge.

The paper is structured as follows: In the first section, a brief overview of the fRPM-fan method is given. Subsequently, its application to the ASPIRE fan concept is discussed in terms of the CFD, fRPM, and CAA setups. In the following section, the results of the cyclostationary fRPM-fan simulations at three different radial positions are shown and the respective influences of wake and background turbulence are analyzed. The aforementioned correction technique is introduced and applied. Lastly, the plausibility of the fan broadband noise prediction is checked by comparing the numerical results to scaled data of two fan rig experiments.

II. Overview of the fRPM-fan method

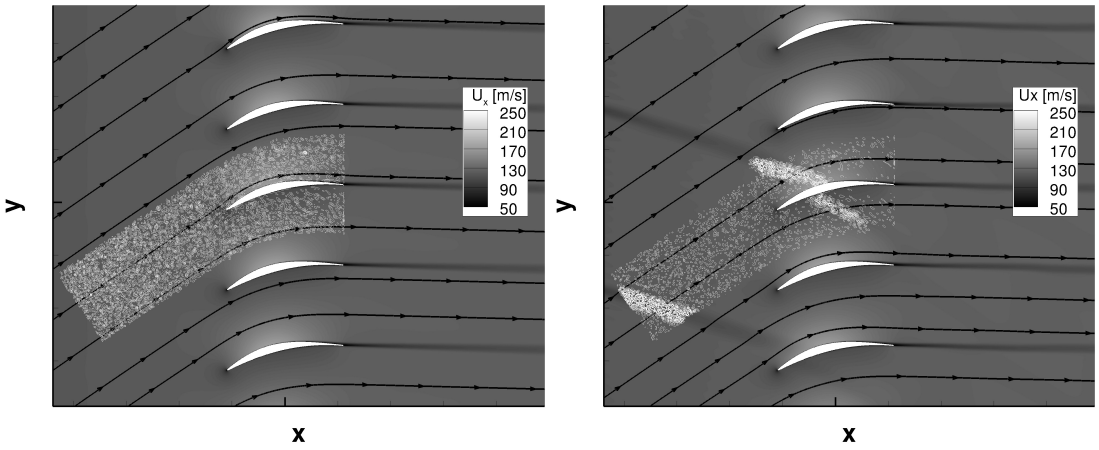

Fig. 1 Comparison of simulations: constant (left) and periodic (right) turbulence statistics and mean flow. Vorticity and axial flow velocity shown.

The fRPM-fan method denotes a fRPM-based synthetic turbulence method that is applied for fan broadband noise predictions. The method is essentially a hybrid method consisting of three different methods: the Computational Fluid Dynamics (CFD) method, the fast Random Particle Mesh (fRPM) method, and the Computational AeroAcoustics (CAA) method.

A URANS simulation provides the mean flow and turbulence statistics required as inputs by the fast Random Particle Mesh (fRPM) method and the Computational AeroAcoustics (CAA) code. The fRPM method is a fast implementation of the Random Particle Mesh Method as introduced by Ewert [12] and uses recursive filters on Cartesian grids to speed up simulations [13]. For fan applications, the fRPM method is used to synthesize time-space-dependent turbulence upstream of the stator vanes. It works as follows: White noise is scaled by a local variance, i. e. a turbulent kinetic energy k_t, and then spatially filtered to realize a local turbulent length scale Λ. Several Gaussian filters of different length scale can be superposed to realize a realistic target spectrum [14], e. g. a von Kármán spectrum. The variance of each Gaussian filter depends on an analytical weighting function.

The synthesized turbulence is coupled into the CAA domain by adding a relaxation term to the momentum equations as proposed by Ewert et al. [15]. The CAA solver PIANO [16] is used to compute the convection of the synthesized turbulence, the sound generation, and the sound propagation. For this work, the low-dispersion low-dissipation Runge-Kutta method [17] was used

for the time integration and the dispersion-relation-preserving finite difference scheme by Tam and Webb [18], for the spatial discretization. The code was applied to solve the linearized Euler equations as the effect of non-linearities was shown to be negligible for this case [19].

The synthesized turbulence injected into the CAA domain propagates with the mean flow and interacts with the stator leading edge, where it generates broadband noise. The CAA propagates the sound to the sensor positions at which the generated sound can be evaluated in terms of sound power or sound pressure.

The fRPM-fan method was extended by Wohlbrandt et al. [10] to enable the consideration of cyclostationarity. The wake can thus be reconstructed at each simulated time step in terms of the local turbulent kinetic energy k_t, the local turbulent length scale Λ, and the local mean velocity u_0. While it is technically possible to investigate the cyclostationarity of these variables separately [10], it was not done in this paper. For simplicity's sake, simulations that consider cyclostationarity in its mean flow and turbulence statistics are described as "cyclostationary" or "periodic". Simulations that do not consider cyclostationarity and instead rely on circumferentially averaged values are referred to as "steady" or "constant". Examples for both types of simulations are shown in Fig. 1.

III. fRPM-fan method applied to the ASPIRE fan

The fRPM-fan method was applied to the ASPIRE fan configuration. The target bypass ratio is 16 and the in-flight minimum engine thrust was chosen to be comparable to a typical engine of a modern, mid-sized passenger aircraft with two underwing engines. The fan stage features a cut-off design of the blade passing frequency tone with 16 rotor blades and 36 OGV's. Details regarding the design characteristics and approach operating conditions at approach are given in Table 6. The work of Schnell et al. [1] features an in-depth discussion of the design and optimization of the ASPIRE fan stage.

In this section, the test matrix and the setups of the individual methods needed for the study of fan broadband noise, namely CFD, CAA, and fRPM, are discussed.

A. Definition of test matrix

Seven different simulations are discussed in this paper. An overview of these simulations is given in Table 2. The identifiers introduced in Table 2 are used to denote the simulations during the

Table 2 Test matrix of simulated configuration

identifier	description	cyclostationary?
P-20	at 20% stator height	yes
P-50	at 50% stator height	yes
P-80	at 80% stator height	yes
C-50	spectrally averaged TLS	no
C-50-3P	three vortex source regions	no
C-50-wake	wake TLS and TKE	no
C-50-background	background TLS and TKE	no

course of this work. The first three simulations investigate the fan broadband noise at three different spanwise positions. Cyclostationarity was considered and linearized Euler equations were applied. The three simulations were performed to improve the fan broadband noise prediction using the 2D technique. The other simulations were done to further investigate the influence of cyclostationarity by quantifying the contributions of ingestion and rotor-stator-interaction noise (C-50-background and C-50-wake) to the overall fan broadband noise. The simulation denoted as C-50-3P features three vortex source regions exciting three instead of just one stator vane as for the C-50 simulation to check the assumption of acoustically uncorrelated vanes.

The three positions located at 20%, 50%, and 80% of the stator height are shown on a slice in the rotor domain (see Fig. 2). The axial positions of the slice was chosen to be located in the rotating domain of the 3D RANS computation roughly in the middle of the interstage section. The TKE and TLS contours are shown. The spanwise positions were chosen to be representative of the entire duct, while avoiding the wall boundary layers and areas of flow separation near the hub and tip walls of the duct.

In this work, cases C-50 and C-50-3P both use a spectral averaging technique for determining a turbulent length scale [10, 19], which can be used to approximate the results of cyclostationary simulations. This averaging technique was shown to work best if the turbulence spectral shape closely resembles a von Kármán. While the synthesized turbulence interacts only with one stator vane for simulation C-50, the synthesized turbulence interacts with three stator vanes for simulation

C-50-3P. The simulations were performed to test if assuming acoustically uncorrelated vanes are permissible for the investigated case. In the simulations C-50-wake and C-50-background, the wake and background turbulence were separately investigated.

The computation time for the reference case P-50 amounted to 4.5 days on 11 Intel(R) Xeon(R) CPU's E7-4830 v3 @ 2.10GHz. The computation time depends on the grid size, the largest permissible time step, and the total amount of time steps. The largest allowed time step depends on the smallest cell in the grid and the total amount of time steps was chosen so that all simulations consider at least 50 rotor wakes. If a constant simulation instead of a periodic simulation is performed, the total computation time decreases by about half.

B. CFD setup

CFD simulations are needed to provide inputs in terms of mean flow and turbulence characteristics for the CAA and fRPM methods. The DLR in-house solver TRACE [20] was used to perform all CFD simulations. A MUSCL (Monotonic Upstream Scheme for Conservation Laws) method of second order accuracy based on Fromm's scheme was applied for the spatial discretization and an Euler Backward scheme of second order accuracy, for the time discretization. The SSG/LRR-ω full Reynolds Stress turbulence model [21] was used. The turbulence at the inlet boundary of the fan stage was defined by a turbulence intensity of 1% ($k_t = 1.4\ m^2/s^2$) and integral turbulent length scale of 0.01 m as those numbers are roughly representative in terms of expected magnitude for outdoor and rig testing. Compared to Boussinesq-based two-equation Menter SST k-ω turbulence model (see Figures 2 and 3), the wake structure can be clearly identified in terms of TLS and TKE using the SSG/LRR-ω turbulence model. Upstream of the rotor blades, the ingested turbulence is nearly identical for both simulations. In the interstage region, the TKE in the wake is also quite similar, while some small differences in the background TKE can be observed. The TLS of the Menter SST k-ω turbulence model appears to be smeared and is too low in large regions between the wakes. This has a potential influence on the fan broadband noise, in particular the contribution of the background turbulence.

For this paper, a 3D RANS and three q3D URANS simulations at approach conditions were performed. The 3D RANS simulation is needed to extract streamlines at the chosen spanwise to set

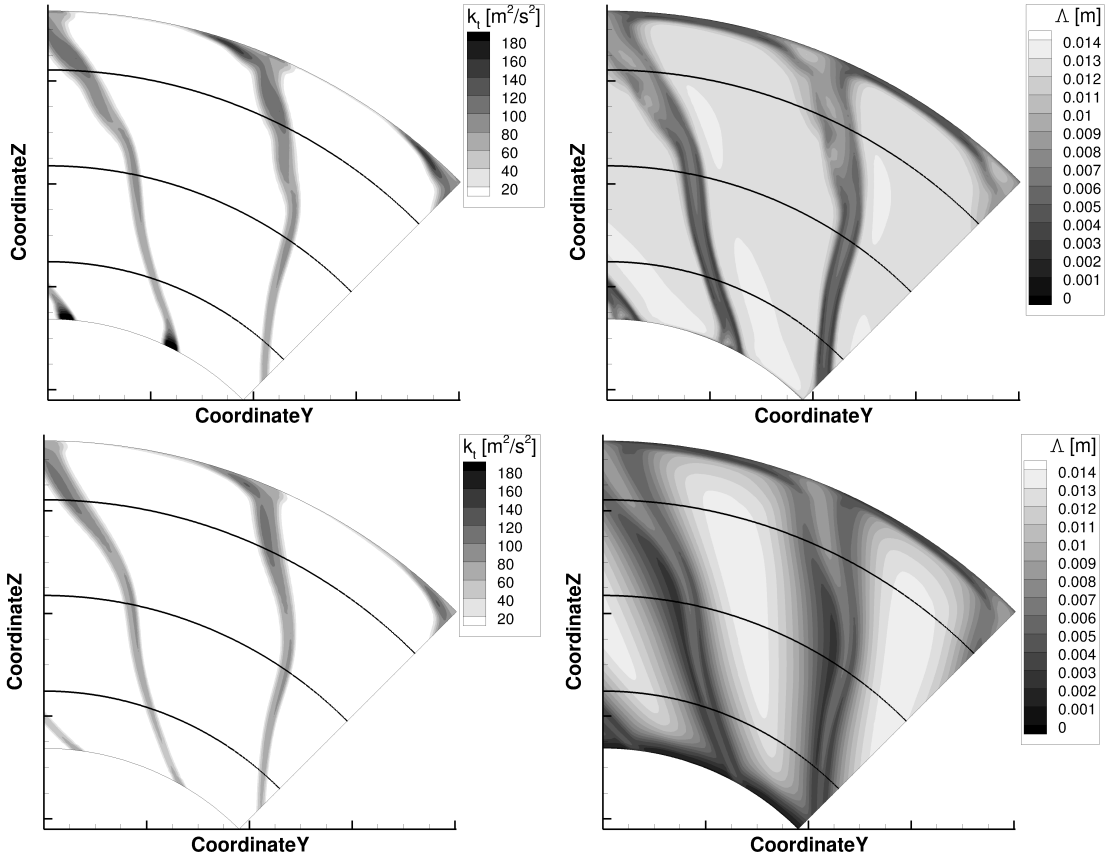

Fig. 2 Slices showing the rotor wake in the rotating domain of the 3D RANS simulation. Contours of the turbulent kinetic energy k_t (left) and of the integral turbulent length scale Λ (right) are shown for the SSG/LRR-ω Reynolds Stress (top) and Menter SST k-ω (bottom) turbulence models. Lines indicate the streamtraces corresponding to 20%, 50%, and 80% of the stator height.

up the q3D URANS simulations (see Fig. 4). Periodic boundary conditions were applied to the q3D URANS simulations. Thus, the URANS simulations contained four rotor and nine stator blades. In the stator domain, unsteady solutions of the first 15 harmonics were needed to correctly reproduce the wake structure in the absolute domain of reference. The number of required harmonics mainly depends on the flow gradients; more harmonics are needed to resolve steeper gradients. In the stator domain, the mean flow, i.e. the 0th harmonic, is obtained via a flux averaging between the moving frame of reference of the rotor block and the absolute frame of reference in the stator block. For constant cases (C-50, C-50-3P, C-50-wake, C-50-background), only the 0th harmonic was considered.

The q3D domains closely resemble 2D flows. The rotor wake is only dependent on the incidence

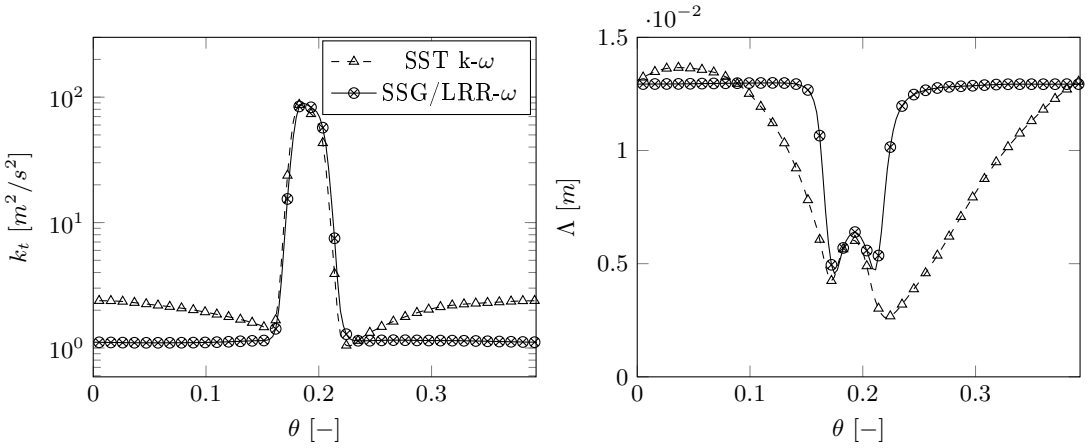

Fig. 3 Wake structure shown in terms of the turbulent kinetic energy k_t (left) and of the integral turbulent length scale Λ (right) for the SSG/LRR-ω Reynolds Stress (top) and Menter SST k-ω (bottom) turbulence models at the streamline position of 50% stator height. Values are extracted from the slices shown in Fig. 2.

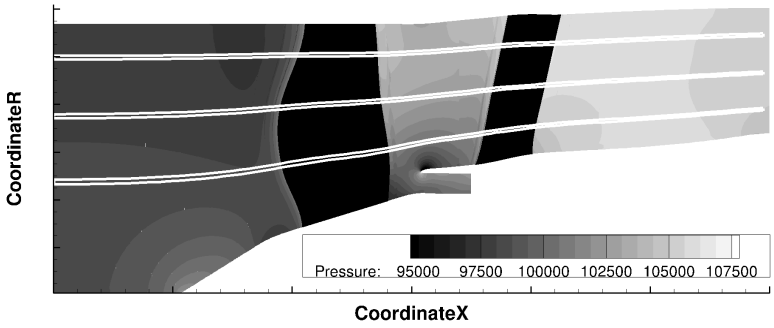

Fig. 4 Q3d URANS domains shown in the fan stage. The contour shows the pressure distribution of the 3D RANS computation.

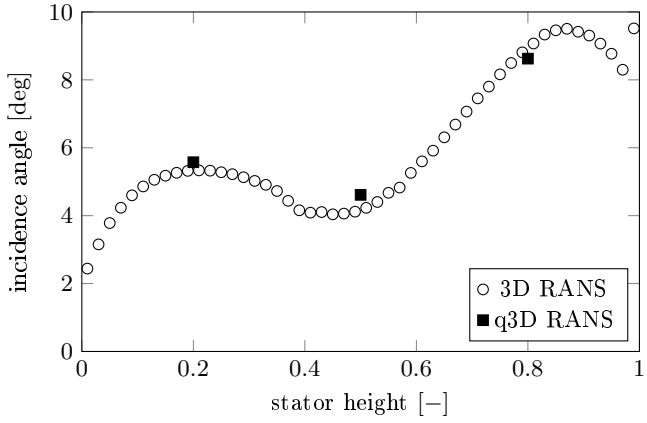

Fig. 5 Flow incidence angles at the rotor leading edge shown for 3D RANS and q3D URANS computations at equivalent streamline positions.

angle of the rotor blade. Hence, the operating point of the q3D URANS simulations were set to match the incidence angle of the 3D RANS at the equivalent streamline position. The incidence angles of the rotor are shown in Fig. 5. The offset in incidence angles between URANS simulations and the 3D RANS computation is small. Of course, 3D effects were thus neglected in the q3D simulations. A correction that considers 3D flow effects is introduced in Section IV C.

The mesh design for both 3D and q3D simulations was based on the standard mesh presented by Guérin and Holewa [22]. The only difference to that mesh is that more points were added in the boundary layers at the hub and tip walls for the 3D case in order to fully resolve these boundary layers. Guérin and Holewa [22] performed a mesh study comparing their standard mesh (5.9 million cells in the rotor block and 1.6 million cells in the stator block) to a finer mesh (20.3 million points in the rotor block and 4.8 million cells in the stator block). They used tonal sound power levels in the bypass and inlet duct to evaluate these meshes and found less than 1 dB deviation at each investigated axial position. They concluded that their standard mesh is already suitably well resolved. As the tonal sound power is a highly grid-sensitive variable and the aim of the CFD simulations performed for this study is "only" a correct realization of aerodynamics instead of acoustics, the authors have chosen to use a grid design based on the standard mesh of Guérin and Holewa [22].

C. CAA/fRPM setup

Figure 6 shows an exemplary CAA setup for predicting the fan broadband noise of the ASPIRE fan with the fRPM method. The setup at 50% of the stator height contains the positions of vortex source, vortex sink, sponge zones, and sensors relative to the stator vanes.

The vortex source is an fRPM patch that injects synthetic turbulence into the CAA domain about two chord lengths upstream of the stator leading edge. The fRPM patch was rotated into the direction of the flow so that no buffer zone accounting for the lateral convection was necessary. The region of the patch that actively produces turbulence spans exactly one pitch; the rest of the patch area contains safety margins. It is assumed that the vanes are acoustically uncorrelated and that it is therefore permissible to excite only one blade. The plausibility of this assumption for the ASPIRE fan is shown in the appendix V. The remaining vanes only ensure the correct acoustic radiation due

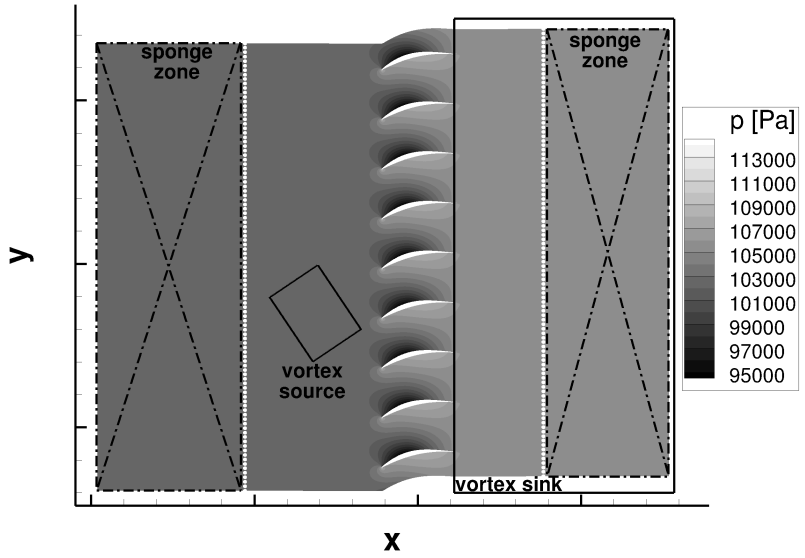

Fig. 6 CAA setup with nine stator vanes at 50% stator height. Sponge zones, vortex source, and vortex sink are shown. White dots indicate sensor positions and the countour plot shows the pressure of the mean flow.

to cascade effects. The CAA domain contains nine instead of 36 vane blades. Periodic boundary conditions are still valid. As a consequence of this choice, the pressure field is constrained into azimuthal mode orders that are multiples of 4 compared to a full-annulus calculation. The effect is most noticeable at low frequencies as the first high-order cut-on mode is of azimuthal mode order 4. At high frequencies, this has almost no impact on the results as demonstrated by Wohlbrandt et al. [10] and Kissner et al. [23].

While the boundary layers were fully resolved in the CFD simulations, the boundary layer is under-resolved in the CAA domain. Neglecting the mean flow boundary layer entirely can lead to the generation of artificial sound at a blunt trailing edge (TE). As vortices move along the surface, they create sound when interacting with the blunt TE. The boundary layer prevents the direct interaction between the TE and the vortices as the vortices are pushed further away from the surface, which reduces the trailing edge noise radiation.

The vortex sink uses the LEE-relaxation method to remove vortices downstream of the stator trailing edges. The vortices tend to interact with the stator wake resulting in hydrodynamic pressure fluctuations. As only the acoustic pressure fluctuations are of interest, the vortices are removed by setting the target vorticity to zero.

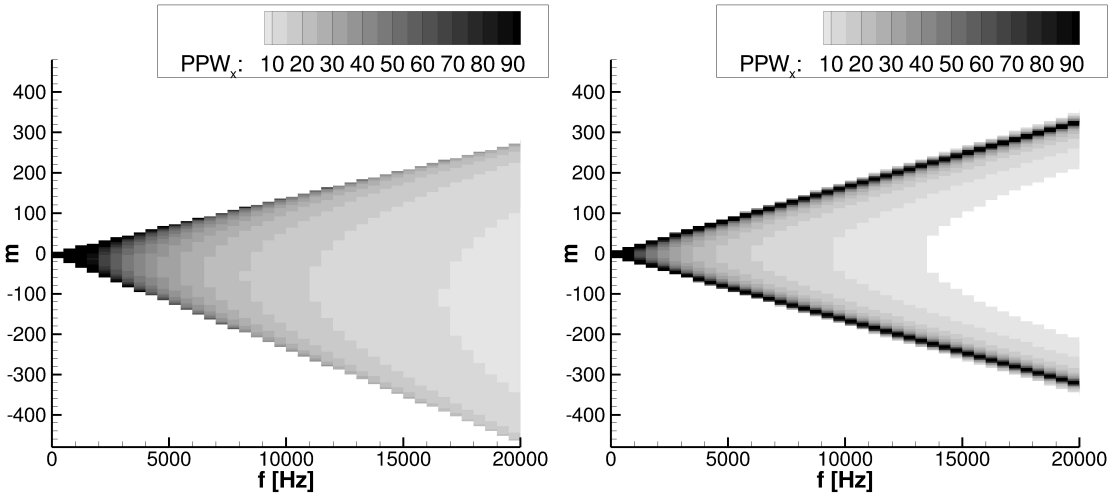

Fig. 7 Acoustic resolution in terms of points per wavelength for cut-on acoustic modes shown for the simulation at 50% of the stator height. As the duct was reduced to 9 stator vanes, only azimuthal modes that are multiples of 4 are included. Upstream propagating modes are shown on the left and downstream propagating modes, on the right. White areas within the cut-on cone mark modes, where the axial resolution is less than the targeted 7 PPW.

Sponge zones were placed at the in- and outlet boundaries to avoid acoustic reflections. An additional cell stretching - not exceeding a value of 1.1 - was applied.

The sensors were equally spaced up- and downstream of the stator. At these positions, sound power levels were computed under the assumption that the 2D simulation at a given stator height is representative for the entire duct and that the blades are acoustically uncorrelated [10].

High-order spatial discretization schemes require a high grid quality in the computational domain. The chosen grid resolution depends on two factors: acoustics and turbulence.

1. Acoustic mesh resolution

The CAA mesh was designed to propagate sound waves up to a frequency of 10 kHz without significant dissipation. A maximum grid size of $dx_f = 0.00486$ m was chosen. The minimal acoustic resolution was chosen to be 7 points per wavelength (PPW), which complies with the theoretical resolution limit of 5.4 PPW for a Dispersion-Relation-Preserving (DRP) scheme [24]. A 2D, low-swirl approximation was used to identify all cut-on modes in the duct and to determine their wave lengths in order to calculate the resolution of each azimuthal mode. Fig. 7 shows the axial resolution of up- and downstream propagating acoustic modes for the simulation at 50% of the stator height.

White areas within the cut-on cone indicate a resolution level below 7 PPW. As can be seen, the chosen resolution complies with the target frequency of 10 kHz. In pitchwise direction, the mesh design adheres to the more stringent requirements for resolving turbulence. The number of pitchwise points per stator passage are 55 at 20%, 66 at 50%, and 107 at 80% of the stator height ensuring the resolution of azimuthal mode orders of up to 282, 339, and 550 respectively. The acoustic resolution is therefore less critical in pitchwise than axial direction and complies with the target frequency. Note that as the critical cell size upstream of the stator vanes also depends on the turbulence rather than acoustics, a smaller cell size (to discussed in the subsequent paragraph) was assumed for the upstream propagating modes.

2. Turbulent mesh resolution

Upstream of and in the proximity of the stator vanes, the grid was designed to resolve the injected, synthesized turbulence up to the target frequency. For the investigated case, the turbulent grid resolution requirements are more stringent than those imposed by acoustics.

The used turbulent grid resolution was designed according to a conservative best practice procedure. The von Kármán spectra were realized by the superposition of seven Gaussian turbulence spectra in the fRPM domain and the chosen cell sizes ranged between 0.00100 m and 0.00125 m for all simulations. The resolution of the wake turbulence is most critical for the turbulent resolution as the turbulent length scale are smaller in the wake than in background shifting the peak frequency towards higher frequencies. In section IV A 1, it is shown that the chosen grid resolution is well suited for resolving the turbulence up to at least a frequency of 10 kHz. As the turbulence as well as the pitch is different at all spanwise positions, different grids ranging between 103,824 and 174,092 cells per passage needed to be used.

IV. Results and discussion

In the following section, the results of the test matrix are discussed. At first, the cyclostationary simulations at different spanwise positions were analyzed. The simulations were performed using linearized Euler equations and considering the cyclostationarity in the mean flow and the turbulence statistics. The contribution of wake and background turbulence to the overall stator broadband noise level is then analyzed in detail for the simulation at 50% of the stator height. In a next step, a

correction technique is introduced to account for 3D flow effects and the wake development between vortex source and the stator leading edge. The corrections are then applied to all simulations. Lastly, the numerical results are compared to scaled, experimental data.

A. Fan broadband noise at different spanwise positions

To determine the fan broadband band noise, the cyclostationary simulations at 20%, 50%, and 80% of the stator height are evaluated in terms of the velocity frequency spectra to ensure the correct realization of the turbulence and in terms of the sound power.

1. Analytical and numerical velocity frequency spectra

Averaged, analytical transverse velocity frequency spectra as well as the local spectra at circumferential positions within one rotor passage are shown in Fig. 8. For the different duct heights, the contribution of background and wake turbulence to the overall turbulence can also be seen. Spectra with lower peaks at lower frequencies can be directly attributed to the background turbulence, while spectra with higher peaks at higher frequencies can be attributed to the wake turbulence. For this configuration without any applied corrections, it can be said that the background turbulence dominates at lower frequencies and the contribution of the wake turbulence starts at a frequency of 1 kHz. Furthermore, it can be noticed that the influence of the wake turbulence is largest at a stator height of 20% and smallest at a stator height of 80%.

A sensor was positioned in the vortex source region and transverse velocity frequency spectra were determined. A comparison with the averaged analytical spectra shows that the fRPM method is able to reproduce these spectra (see Fig. 9). This indirectly proves that the fRPM method is capable of synthesizing the prescribed, cyclostationary turbulence. The figure also shows that the intended resolution of turbulence up to a frequency of 10 kHz was achieved by all simulations.

2. Sound power level frequency spectra

The raw power spectra up- and downstream of the fan are shown in Fig. 10. No corrections have been applied yet and the grey areas in the graphs indicate the limit of the mesh resolution. In

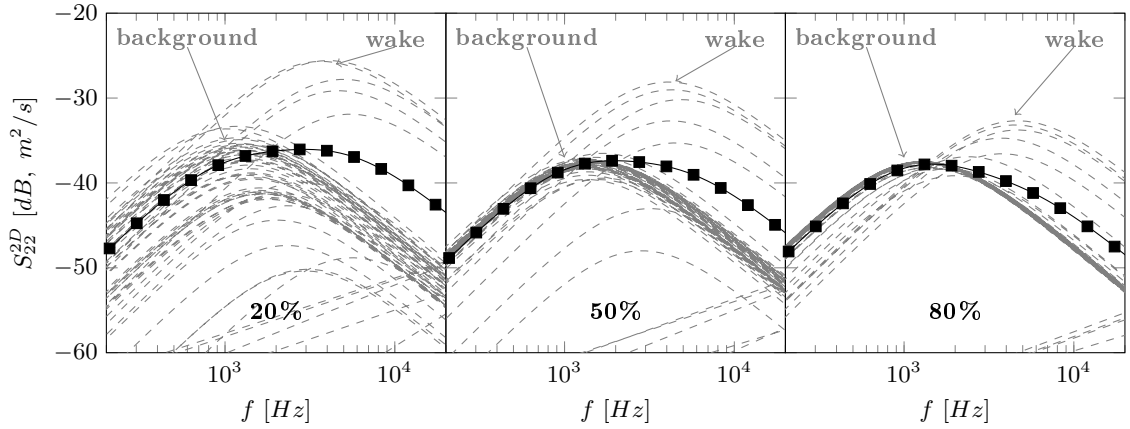

Fig. 8 Averaged transverse velocity frequency spectra shown by black, solid lines. Gray, dashed lines show local transverse velocity frequency spectra calculated at circumferential positions within one rotor passage.

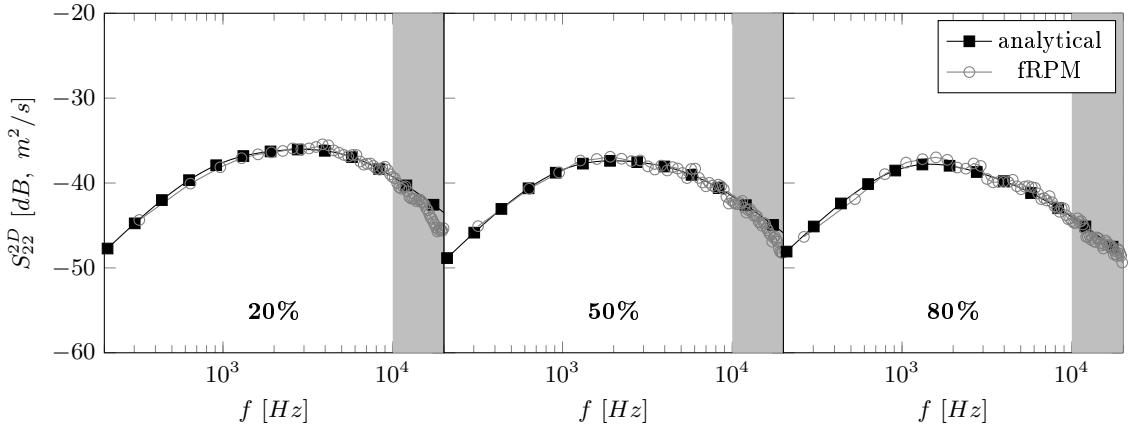

Fig. 9 Upwash velocity frequency spectra realized by the fRPM method compared to respective analytical spectra. The gray boxes indicate the limit of the mesh resolution.

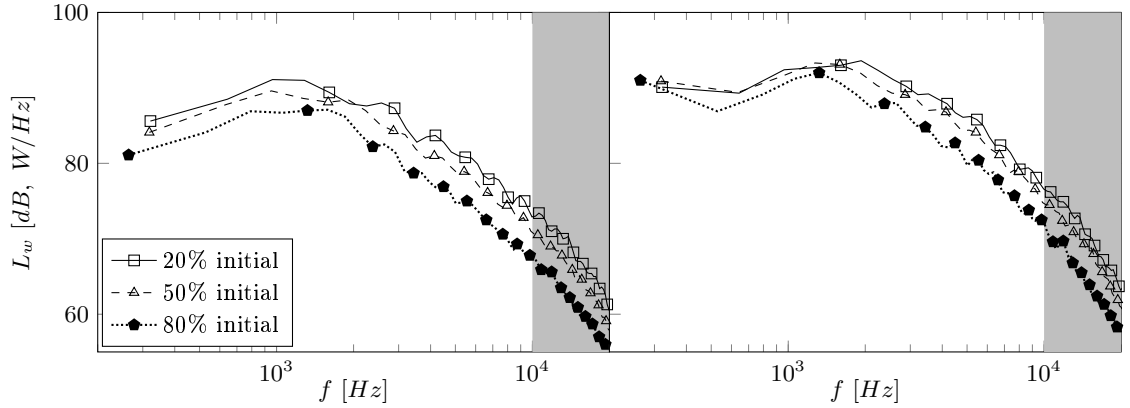

Fig. 10 Initial power spectra upstream (left) and downstream (right) of the stator row at all spanwise positions.

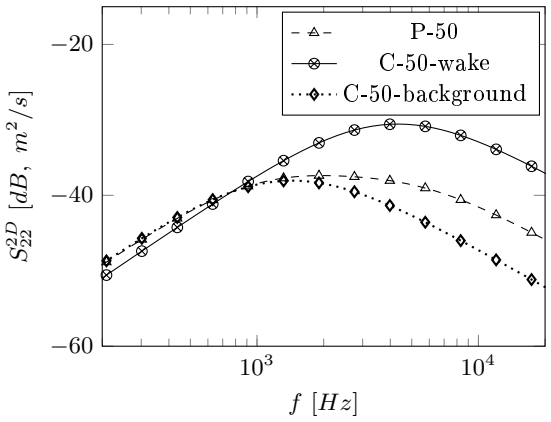

Fig. 11 Analytical, 2D upwash velocity frequency spectra for simulations P-50, C-50-wake, and C-50-background.

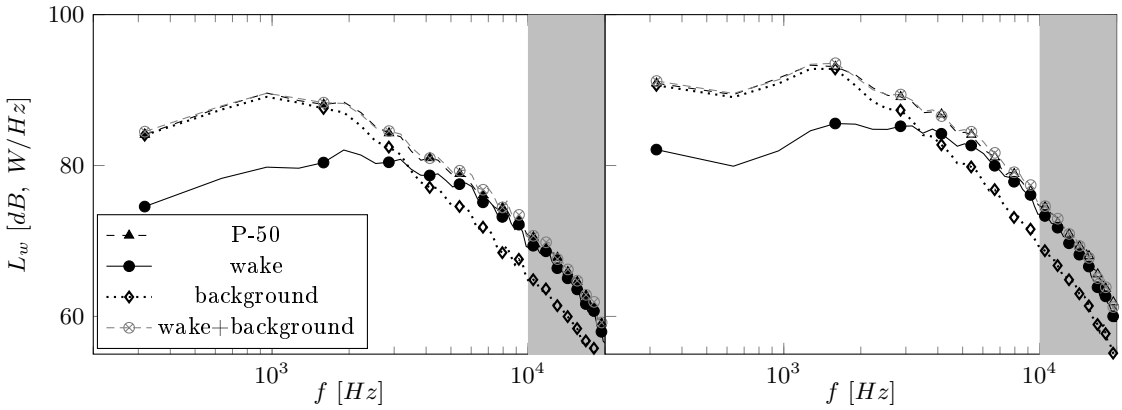

Fig. 12 Power spectra upstream (left) and downstream (right) of the stator row showing the contribution of wake and background turbulence to the overall fan broadband noise level.

that area, some dissipation effects can be expected.

B. Contribution of wake and background turbulence to the overall fan broadband noise

The averaged upwash velocity frequency spectrum of the P-50 simulation results from a superposition and averaging of all locally realized spectra spanning a rotor passage. It thus contains contributions that belong to the background turbulence and contributions that belong to the wake turbulence. In this section, the influence of these two noise generation mechanisms - ingestion and RSI noise - on the overall fan broadband noise is studied by performing two additional simulations, which consider wake and background turbulence separately.

To determine an upwash velocity spectrum characterizing wake turbulence, all spectra within

Table 3 Uncorrected contribution of wake and background turbulence to the overall fan broadband noise.

identifier	$OAPWL_{up}$ [W]	$OAPWL_{up}$ [%]	$OAPWL_{down}$ [W]	$OAPWL_{down}$ [%]
wake	0.58	30.4	1.63	33.1
background	1.33	69.6	3.29	66.9
total	**1.91**		**4.92**	

the wake were summed up and averaged. The same procedure was applied to determine an upwash velocity spectrum, which describes the background turbulence. The resulting spectra along with the spectrum of the cyclostationary P-50 simulation are shown in Fig. 11. The P-50 spectrum is a combination of the C-wake and C-background spectra. Therefore compared to a typical von Kármán spectrum, the P-50 spectrum has a much flatter peak. The C-background spectrum has its peak frequency close to 1.5 kHz, while the C-wake spectrum peaks at a frequency of about 4.5 kHz. The turbulence in the wake causes an increase in amplitude of the averaged velocity frequency spectrum at higher frequencies. The averaged upwash velocity frequency spectrum S_{22}^P can be described in terms of its background S_{22}^b and wake S_{22}^w components as follows:

$$S_{22}^P = \widetilde{\theta_w} S_{22}^w + \left(1 - \widetilde{\theta_w}\right) S_{22}^b, \tag{1}$$

where the non-dimensional wake width $\widetilde{\theta_w}$ can be expressed as a function of the wake width θ_w in terms of a circumferential angle and of the number of rotor blades B: $\widetilde{\theta_w} = \frac{\theta_w}{\frac{2\pi}{B}}$. It appears that the background and wake turbulence spectra nearly have a von Kármán shape. Thus, the respective TLS and TKE can be determined by fitting the spectra.

The determined turbulence statistics are prescribed as inputs for simulations C-50-wake and C-50-background. The results of the acoustic simulations are depicted in Fig. 12. Note that the weighting is already considered and therefore the real contribution of wake and background turbulence to the overall fan broadband noise are depicted in this figure. The rotor-stator-interaction noise resulting from the wake turbulence only has a significant contribution in the high frequency range, while the ingestion noise is dominant at lower frequencies. The cyclostationary sound power level spectra is equivalent to the weighted contributions due to wake and background turbulence as

shown in Fig. 12:

$$L_W^P = 10 \log \left(\frac{\widetilde{\theta_w} P_w + \left(1 - \widetilde{\theta_w}\right) P_b}{P_{ref}} \right). \tag{2}$$

The overall sound power can be determined analogously. The overall sound power was determined in a frequency range between 500 Hz and 10 kHz and was used to quantify the contribution of RSI noise, which is caused by the wake turbulence, and the contribution of ingestion noise, which is caused by the background turbulence (see Table 3). The evaluation of the overall sound powers shows that the fan broadband noise is about 70% ingestion noise and 30% RSI noise. The assumption that the RSI noise is the dominant source in fans is therefore not valid for the investigated case - at least as long as no corrections are considered. In fact, the influence of ingestion noise is more critical for the overall fan broadband noise. Thus, both wake and background turbulence have to be considered for the studied fan, which supports the choice of including cyclostationarity in the simulations discussed in Section IV A.

It should be noted that the level of background turbulence - and therefore ingestion noise - depends on the chosen turbulence characteristics at the engine inlet and on the distance from the rotor trailing edge. In this case, the inflow turbulence statistics were chosen to be representative of testbed conditions. If a lower turbulence intensity and a smaller length scale were prescribed, the relevance of ingestion noise would decrease. In addition, the distance from the rotor trailing edge has an influence. If the background turbulence level is not negligibly small, its relative contribution to the overall fan broadband noise increases with an increasing distance from the rotor trailing edge as the wake turbulence fades.

C. Corrections for 3D flow effects and wake development

In the following section, a correction technique will be introduced and applied to the sound power levels to solve the shortcomings identified in previous studies.

1. Correction technique

The two-dimensional CAA simulations at different spanwise positions neglect two effects: (1.) Changes in the wake: The turbulence is directly prescribed at the position of the patch and this

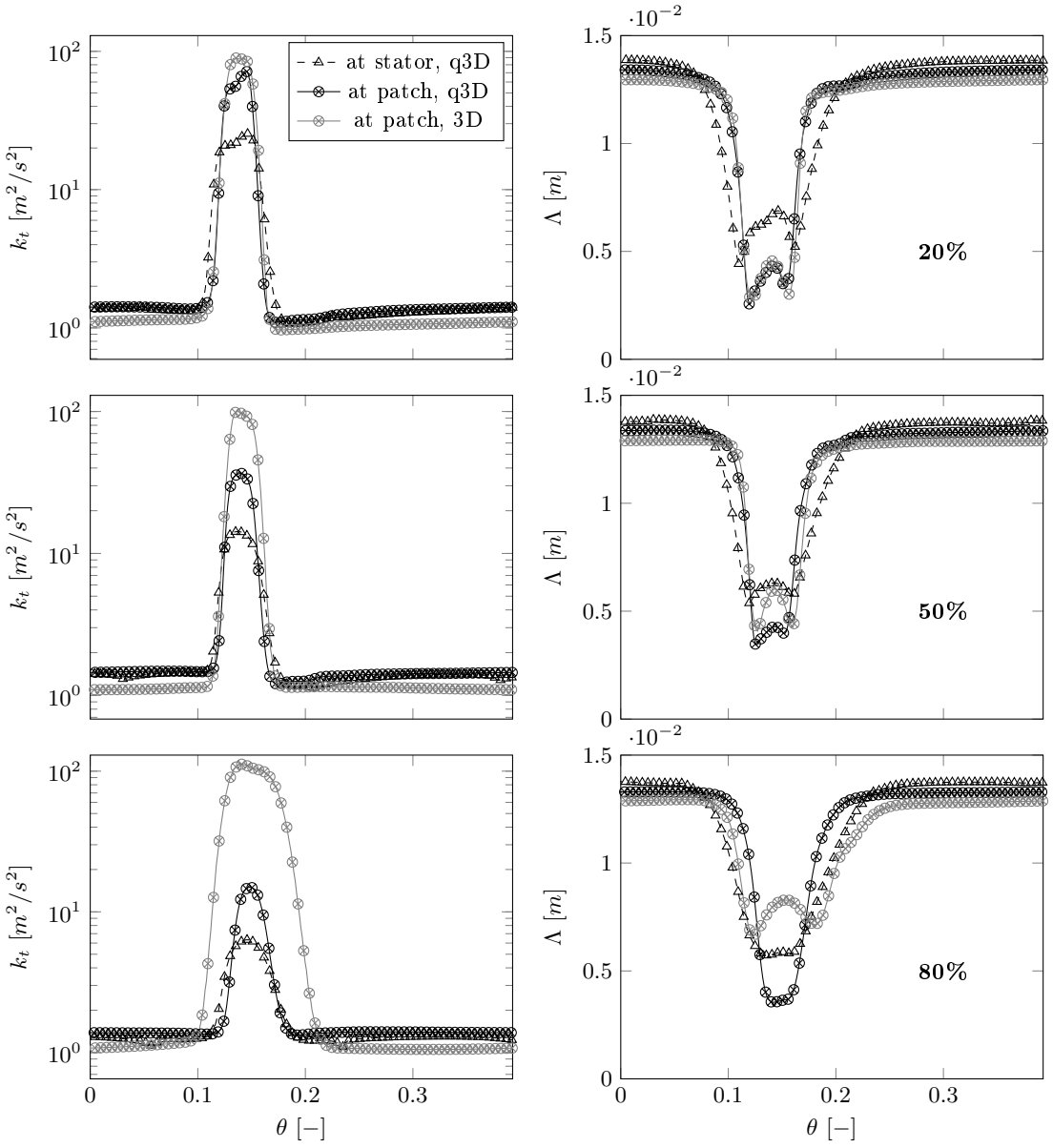

Fig. 13 Wake structures in terms of TKE and TLS at 20%, 50%, and 80% stator height.

prescribed, frozen turbulence interacts with the stator leading edge to produce noise. In reality, the turbulence decays and the wake structure changes as the wake gets more diluted with an increasing distance from the rotor. (2.) 3D flow effects: The q3D URANS simulations cannot consider 3D flow effects. For instance, wake structures can be influenced by spanwise velocities induced by areas of flow separation. Since spanwise velocities cannot exist in a q3D simulation, such phenomena cannot be reproduced. These effects significantly influence the shape of the wake. Fig. 13 depicts wakes extracted from the q3D simulations at stator leading edge and fRPM patch positions as well as

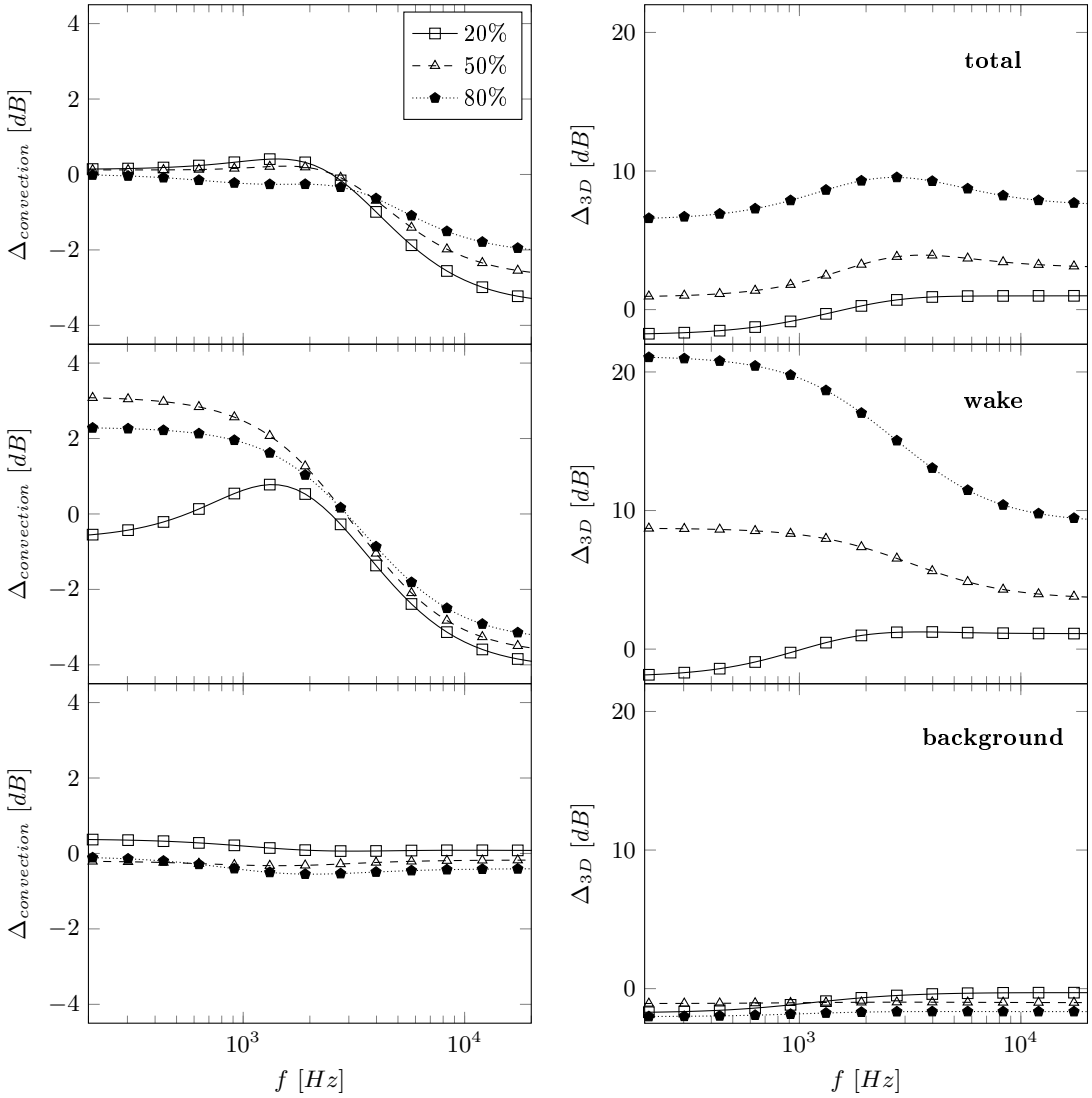

Fig. 14 Correction curves for sound power levels to account for wake changes in the axial direction (left) and 3D flow effects (right) at for the total (top), wake (center), and background (bottom) cases.

wakes extracted from the 3D simulations at the position of the fRPM patch. Significant differences in wake shape and levels of TKE and TLS can be seen. It is necessary to take these differences into account when analyzing the predicted sound power levels. Thus, a correction technique based on the tranverse velocity component, which is widely thought to be most critical for this sound generation mechanism, was developed.

For each wake depicted in Fig. 13, a 2D circumferentially averaged transverse velocity frequency spectrum can be determined. In addition, averaged spectra considering only the contributions of

wake and background turbulence to overall spectrum can be computed. These transverse velocity frequency spectra are shown in Fig. 20 in the appendix. The figure shows that the background turbulence of the q3D and 3D simulations is nearly identical. The largest changes can be seen in the contribution of wake, which then explains nearly all of the offsets seen in the total spectra. Between the leading edge and patch positions of the q3D simulation, wake TKE levels decrease causing the spectral levels to decrease slightly and the TLS increase causing the peak frequency of the spectra to shift to lower frequencies. The largest change can be seen when comparing the wake contributions of q3D and 3D simulations. The level of the TKE increases for all simulations. While the TLS remains similar at 20% and 50% of the stator height, the TLS increases significantly at 80% of the stator height, which explains the shift in peak frequency.

To describe these effects due to wake development and 3D flow, the difference in transverse velocity frequency spectra between the 3D and q3D simulations at the patch position and between patch and LE positions for q3D simulations are computed. These differences give correction curves as a function of frequency as shown in Fig. 14.

2. Corrected sound power levels

In a next step, the correction curves are added to the total sound power levels to estimate the influence of 3D flow effects and wake development. Figure 15 shows the corrected power spectra of the P-20, P-50, and P-80 simulations. The influence of each correction on the sound power spectra at the respective spanwise positions can be seen in the appendix in Fig. 21. When looking at the overall sound power level before and after applying the corrections in Table 4, then the change at 80% of the stator height was most significant amounting to an increase of about 9 dB. At 50% of the stator height, the corrections yielded a 3 dB increase in the overall sound power level. Lastly, the sound power remained nearly constant at 20% of the stator height.

All spectra have been computed under the assumption that the broadband noise at the respective spanwise position is representative for the entire duct. Figure 15 indicates that the fan broadband noise increases with increasing radial height for this configuration at the investigated operating point.

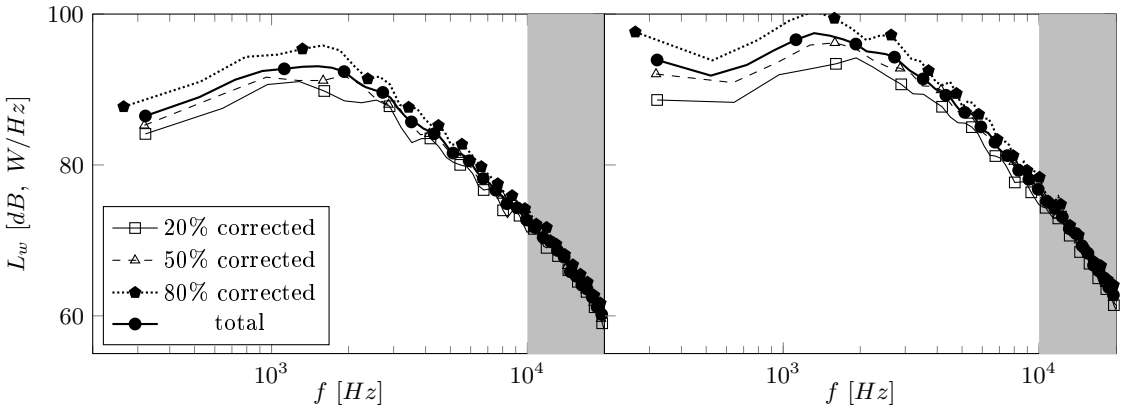

Fig. 15 Corrected and total power spectra upstream (left) and downstream (right) of the stator row at all spanwise positions.

Table 4 Sound power levels up- and downstream of stator row at spanwise positions

stator height [%]	final OAPWL$_{up}$ [dB]	initial OAPWL$_{up}$ [dB]	final OAPWL$_{down}$ [dB]	initial OAPWL$_{down}$ [dB]
20	124.3	124.3	127.9	127.8
50	125.6	122.7	129.8	126.8
80	128.6	120.2	133.0	124.5
Total	**126.6**		**130.8**	

To get a more complete description of the sound power level spectra for the entire fan, the acoustic intensity of the three simulations was averaged and used to compute the sound power:

$$\overline{I_i} = \frac{1}{3}\sum_{n=1}^{3} I_{i,n}. \tag{3}$$

The total sound power level spectra are shown in Fig. 15. While these total sound power level spectra are still only an approximation of the sound power of the entire duct, a more reliable result can be expected using three spanwise positions instead of only one position. The total sound power spectra are close to those at a stator height of 50%. In fact, the total sound power differs by about 1 dB. This indicates that a midspan simulation results in an acceptable approximation for the entire duct if corrections are considered for the investigated case.

Analogous to correcting the overall cyclostationary results, wake and background turbulence contributions to the overall noise levels can also be corrected. The corrected sound power levels at 50% of the stator height are shown in Fig. 16. Compared to the sound power level spectra without

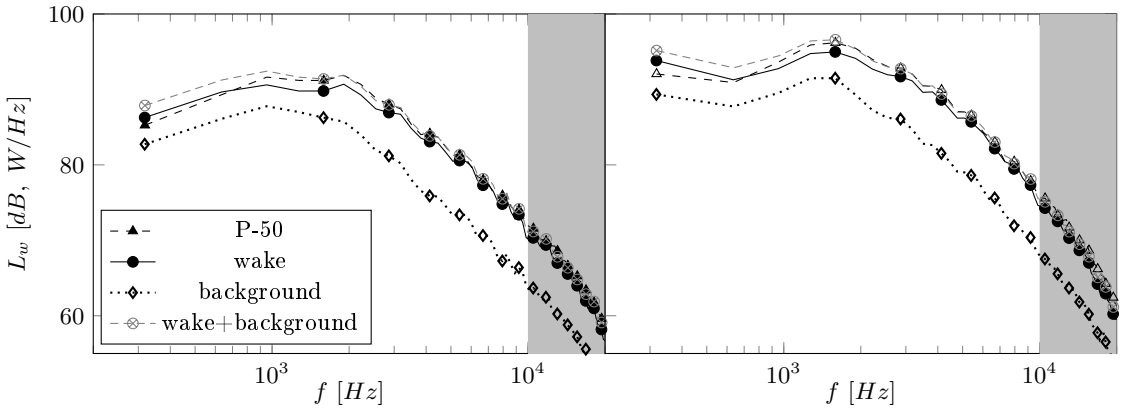

Fig. 16 Power spectra upstream (left) and downstream (right) of the stator row showing the corrected contribution of wake and background turbulence to the overall fan broadband noise level at the stator midspan position.

Table 5 Corrected contribution of wake and background turbulence to the overall fan broadband noise.

identifier	$OAPWL_{up}$ [W]	$OAPWL_{up}$ [%]	$OAPWL_{down}$ [W]	$OAPWL_{down}$ [%]
wake	2.85	74.2	7.46	75.3
background	0.99	25.8	2.45	24.7
total	**3.84**		**9.91**	

correction (compare to Fig. 12), the contribution of wake turbulence is now more relevant. In fact, the overall sound power - integrated over a frequency range between 500 Hz and 10 kHz - indicates that the overall fan broadband noise at 50% of the stator height is comprised of about 25% ingestion noise due to the background turbulence and about 75% rotor-stator-interaction noise due to wake turbulence (see Table 5).

D. Comparison to scaled, experimental data

The ASPIRE fan was designed to be representative of next generation fans. While numerical predictions regarding the noise generation of such engines are insightful and necessary, they are difficult to evaluate as no experimental data for the ASPIRE or any comparable fan design are currently available. The authors decided to tackle this issue by comparing the numerically determined fan broadband noise levels to scaling experimental data of two test cases featuring more conventional

Table 6 Comparison of fan design characteristics and approach operating points of the ASPIRE, ACAT1 and NASA SDT fans

	ASPIRE	ACAT1 (SLS)		ACAT1 (LN)		NASA SDT	
		real	scaled	real	scaled	real	scaled
number of rotor blades	16	20		20		22	
number of stator blades	36	44		44		54	
fan tip radius [m]	1.135	0.428	1.135	0.428	1.161	0.277	0.840
design fan pressure ratio	1.31	1.42		1.42		1.48	
design axial Mach number at fan face	0.59	0.57		0.57		0.59	
approach conditions							
rotational speed [rpm]	1337.8	3828.2	1443.2	3828.2	1410.7	7808.0	2569.1
fan pressure ratio	1.096	1.102		1.093		1.153	
isentropic efficiency	0.931	0.879		0.916		0.855	
axial Mach number at fan face	0.290	0.266		0.285		0.300	
rotor loading	0.341	0.320		0.276		0.274	
mass flow $[kg/m^3]$	420.0	56.5	385.3	60.1	429.3	26.9	243.1
thrust [kN]	18.8	18.7		18.3		18.8	

designs: the ACAT1 [25–27] and the NASA Source Diagnostic Test (SDT) baseline fan [28, 29] at approach conditions. The major advantage of choosing the NASA SDT and ACAT1 fans for this comparison is that a good agreement of the experimental data to numerical results determined using the 2D fRPM-fan method has successfully been demonstrated in previous works [10, 23]. These previous works demonstrate the general suitability of the method for computing fan broadband noise and it is therefore reasonable to assume that the method can also be applied for blind predictions. The comparison is therefore intended to ascertain the plausibility of the numerical results of the ASPIRE fan and to possibly identify common trends between current and future fan designs.

A suitable scaling is necessary as the ASPIRE fan is a full-scale configuration, while the NASA SDT and ACAT1 fans are laboratory fans. The authors chose to introduce a scaling of the test rig data so that the fans produce a similar thrust as the full-scale ASPIRE configuration. The method of scaling is described in more detail in the appendix V. Such scaling procedures are by no means

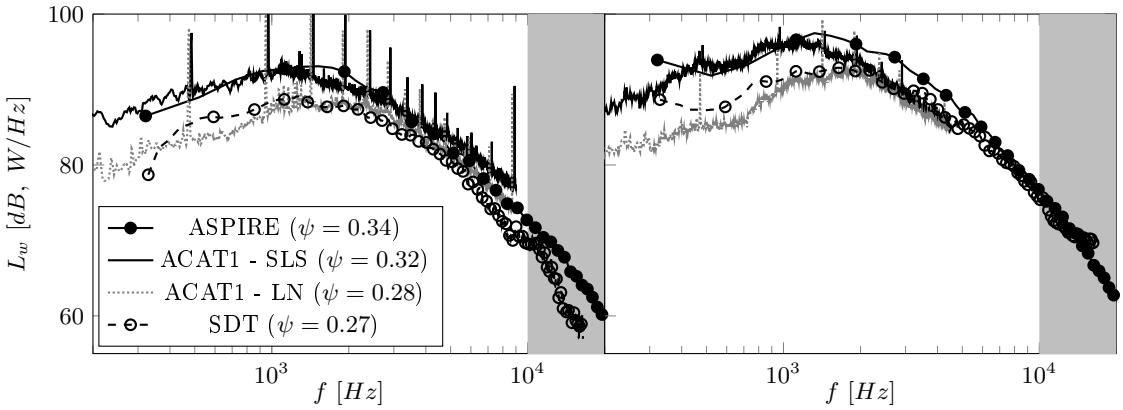

Fig. 17 Comparison of numerical and scaled, experimental power spectra upstream (left) and downstream (right) of the stator row.

unusual as test fans are typically designed to be indicative of the characteristics of an equivalent, full-scale engine. The relevant real and scaled characteristics at the design and at approach operating point are listed in Table 6. For the ACAT1 fan, two approach conditions on two working lines - Sea Level Static (SLS) and Low Noise (LN) - are available. Note that only the bypass flow was considered for the ACAT1 and ASPIRE fan to ensure a meaningful comparison with data from the NASA SDT fan, which does not feature a core flow.

The sound power levels using the scaled, experimental data and the numerical data are compared in Fig. 17. The levels as well as the spectral shapes are in good agreement up- and downstream of the stator vanes, thus confirming the plausibility of the numerically predicted sound power of the ASPIRE fan. Interestingly, the levels mainly depend on the fan loading. In addition, no clear acoustical advantage of the next generation ASPIRE fan compared to the conventional fans can be identified.

V. Conclusion

The main focus of this paper was to study the contribution of ingestion noise - due to background turbulence - and rotor-stator-interaction noise - due to wake turbulence - to the overall stator broadband noise of a next generation fan design at approach conditions. To enable such an investigation, a suitable fan design was chosen and methods capable of considering background, i. e. ingested, turbulence were applied.

Despite the VAN, the ASPIRE fan design is still highly loaded by comparison, which is a result of the highly optimized geometry. An ingestion turbulence of a turbulence intensity of 1% and a turbulent length scale of 1 cm was prescribed at the fan inlet. This turbulence was chosen to be representative of test rig and outdoor testbed conditions in terms of expected magnitude. While the exact turbulence levels depend on the test facility and on weather and terrain characteristics for outdoor tests, the typical turbulence levels tend to be small but non-negligible. The chosen turbulence was therefore ideal for studying the effect of background turbulence, which can be essential for the interpretation of future experimental and numerical studies.

The used numerical method, the 2D cyclostationary fRPM-fan method, was adapted from previous works to ensure the correct realization of the background turbulence and to address some shortcomings of the original 2D method as applied by Wohlbrandt et al. [10]. The SSG/LRR-ω Reynolds Stress turbulence model was applied for the CFD simulations, which are required as inputs for the CAA and fRPM codes. For credible fan broadband noise predictions, simulations were performed at three radial positions instead of just one simulation at the stator midspan position. Additionally, a correction technique based on transverse velocity frequency spectra was introduced to correct for effects that the 2D method does not inherently contain. Firstly, a q3D CFD simulation neglects three-dimensional flow effects. Secondly, the cyclostationary technique reconstructs the turbulence at the position of the vortex source using local turbulence and flow characteristics. The correction is needed to account for the wake development between the vortex source and the stator leading edge. The key findings of this paper are listed below:

- The importance of the background turbulence in terms of fan broadband noise depends on its relative level compared to the wake turbulence and is not necessarily negligible. Once corrections are applied to the simulations at 50% of the stator height, the overall broadband noise is about 25% ingestion noise and 75% rotor-stator-interaction noise. This study indicates that background turbulence may need to be considered when ingestion turbulence levels are similar or higher than the ingestion turbulence studied in this work. Lower ingestion turbulence levels are likely negligible.

- Instead of performing a cyclostationary simulation, two constant simulations that separately

consider wake and background turbulence can be used.

- The averaged sound power levels of the cyclostationary simulations at three different spanwise positions differ only marginally from the sound power levels at the stator midspan position. For the investigated case, a midspan simulation approach yields an acceptable approximation of fan broadband noise.

- A comparison to scaled, experimental data confirm the plausibility of the numerical results as sound power levels and spectral shapes match well. In addition, the levels mainly depend on the rotor loading.

The advantage of the 2D fRPM-fan method is that it enables to study different aspects of the fan broadband noise mechanism. In this case, it enabled the separate study of wake and background turbulence. In addition, it is a fast method consistently yielding reasonable fan broadband noise predictions. The method is therefore suitable for performing blind noise predictions. In the future, the method will be expanded to three-dimensional space. Three-dimensional flow effects can then be directly considered and the influence of ingested turbulence can be further investigated.

Appendix

Calculation of fan loading

The fan loading ψ was estimated using the following formula:

$$\psi = \frac{\Delta H_t}{U_{tip}^2}, \tag{4}$$

where ΔH_t is the specific enthalpy rise calculated in the absolute frame of reference and U_{tip} is the tangential speed at the rotor tip. The enthalpy rise is calculated as follows:

$$\Delta H_t = c_p \Delta T t = T t_2 \left(\frac{\Pi^{\frac{\gamma-1}{\gamma}} - 1}{\eta_{isen}} \right), \tag{5}$$

where c_p is the pressure specific heat constant, Π is the fan pressure ratio, and η_{isen} the isentropic efficiency. All values are provided in Table 6.

Assumption of acoustically uncorrelated stator vanes

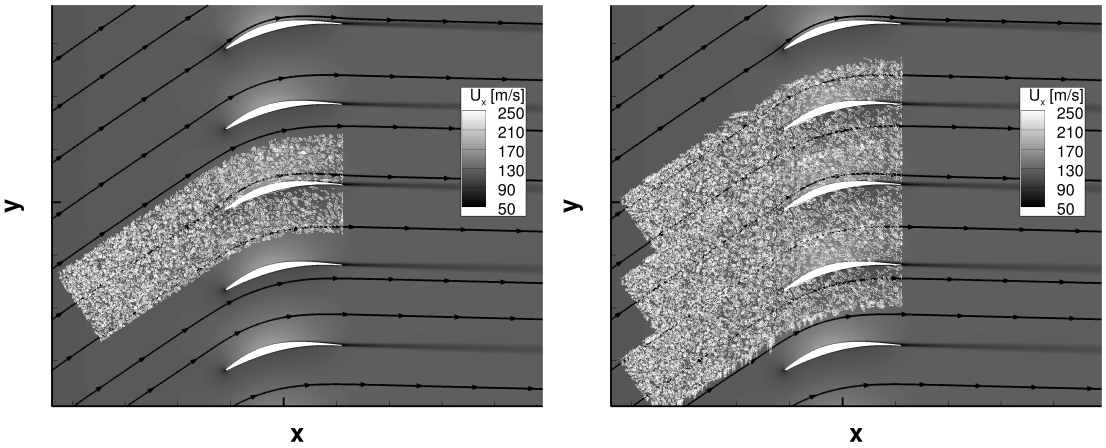

Fig. 18 Comparison of constant simulations C-50 (left) and C-50-3P (right): Vorticity is outlined in white and axial flow velocity contour is shown.

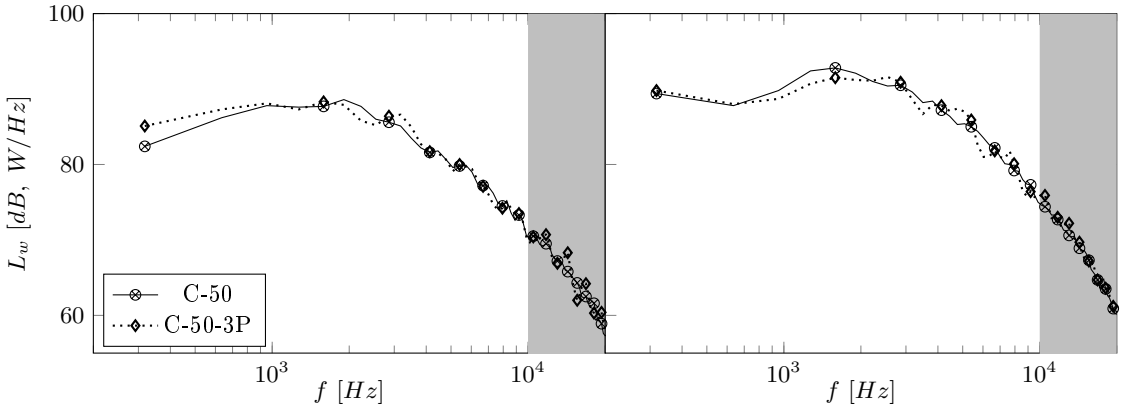

Fig. 19 Power spectra upstream (left) and downstream (right) of the stator row shown for simulations C-50 and C-50-3P.

In this paper, the authors assumed that the stator vanes are acoustically uncorrelated and thus the vortex source regions was designed to produce turbulence, which interacts exactly with one stator vane. To check this assumption, a constant simulation containing three vortex source regions, which span three vane pitches, was performed (see Fig. 18). The results are shown in terms of sound power level in Fig. 19. Except for small deviations at low frequencies in the upstream direction, the levels of simulations C-50 and C-50-3P match well. The assumption of acoustically uncorrelated vanes is therefore permissible for the investigated case.

Upwash velocity frequency spectra used for correction technique

Averaged upwash velocity frequency spectra computed from flow and turbulence profiles, which were extracted from 3D and q3D simulations at patch and stator leading edge positions are shown

in Fig. 20. The contributions of wake and background turbulence to the overall turbulence spectra are also depicted. These correction curves shown in Fig. 14 are computed using the shown upwash velocity frequency spectra.

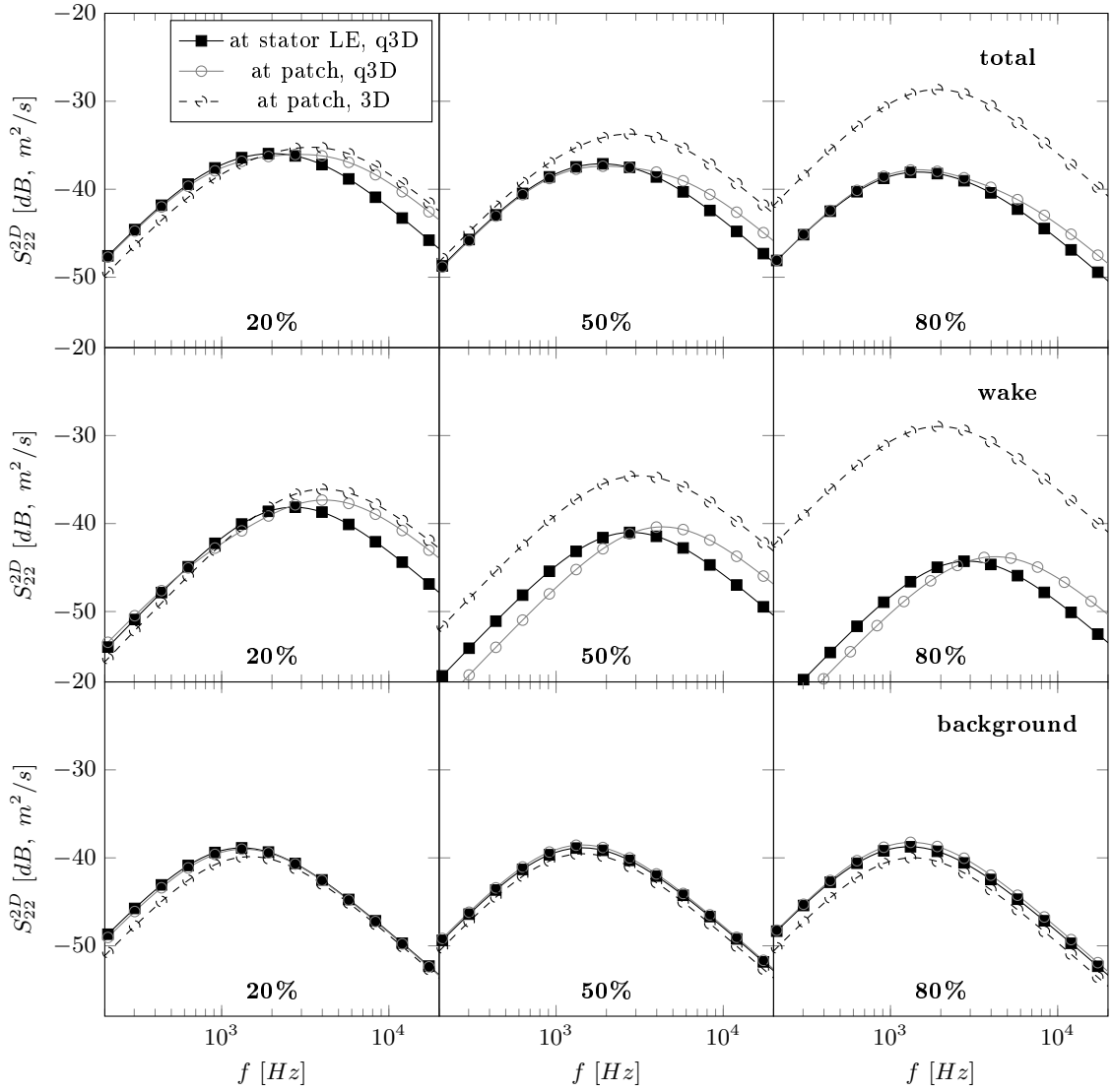

Fig. 20 Upwash velocity frequency spectra at leading edge and patch positions extracted from q3D and 3D simultions. Total (top) circumferentially averaged spectra as well as the contributions of wake (center) and background (bottom) turbulence are shown.

Correction technique applied to sound power level spectra

The correction curves (see Fig. 14) are added to the raw sound power level spectra to correct for 3D flow effects and the wake development between the vortex source and the stator leading edge. While the sound power level spectra at 20% of the stator height is nearly unchanged (see Fig. 21),

the sound power level spectra at 50% and 80% of the stator height are significantly altered - mostly due to the correction for 3D flow effects.

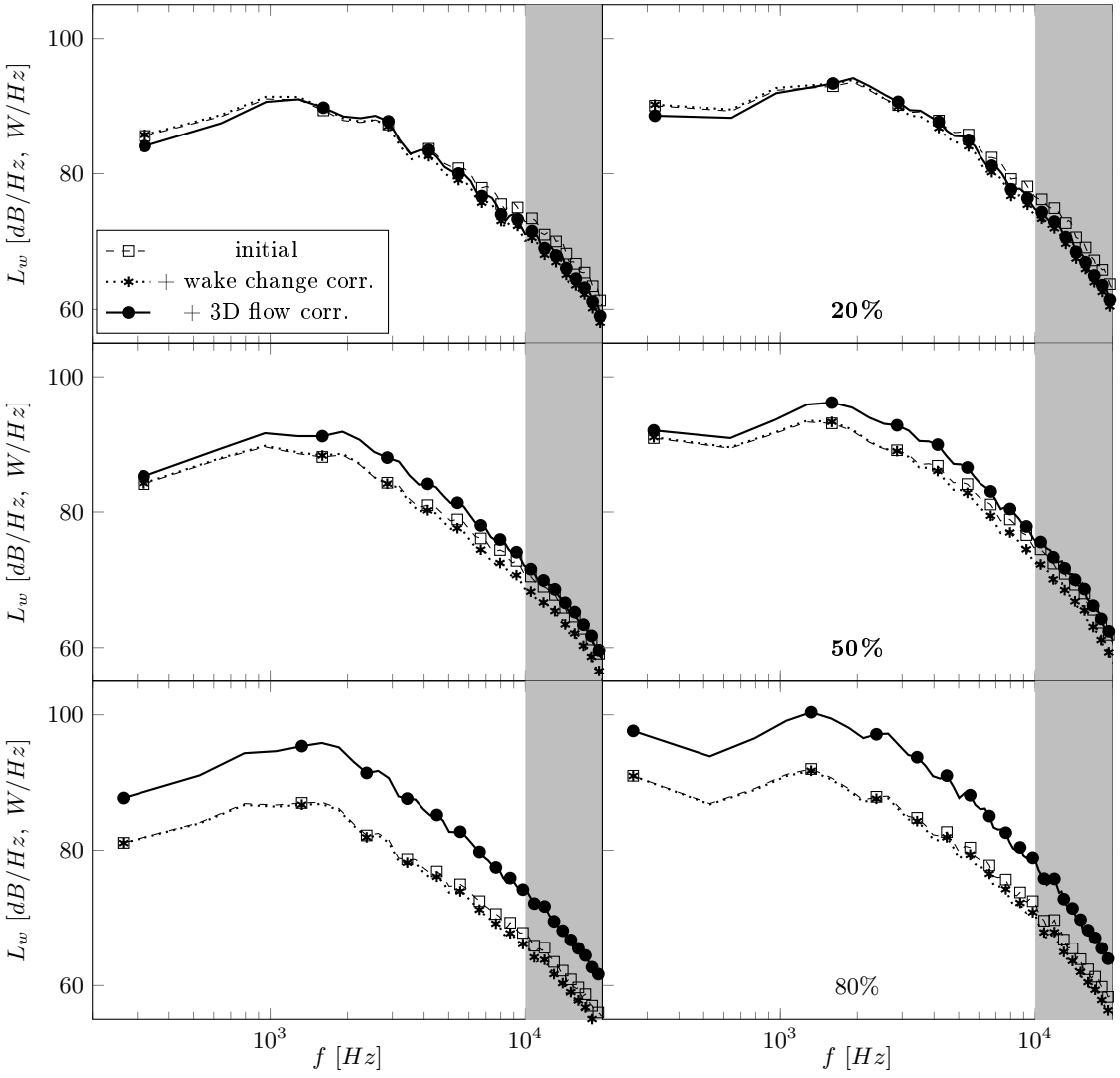

Fig. 21 Power spectra corrections upstream (left) and downstream (right) of the stator row at 20% (top), 50% (center), and 80% of the stator height.

Determination of thrust-based scaling factors

The applied scaling adjusts the diameter of the laboratory fans in order to deliver the same thrust as the full-scale ASPIRE fan at approach conditions.

The core contribution for the ASPIRE and ACAT1 fan were neglected. The bypass flow of the ASPIRE delivers a thrust of 18.8 kN at an altitude of 120 m at ISA conditions at a flight Mach number of $M_0 = 0.23$. The thrust is calculated using the fan pressure ratio, efficiencies, and

prescribed flight conditions. To account for some realistic pressure losses, it was also assumed that inlet and nozzle have an efficiency of 97% and 99% respectively. The geometrical scaling factors β, which describe the ratios between scaled and real fan diameters, is e. g. 3.05 for the SDT fan.

The factor β can be used to correct measured acoustic data of ACAT1 and SDT in terms of frequency and amplitude as follows:

$$f_{scaled} = \frac{f}{\beta}, \tag{6}$$

$$PWL_{scaled} = PWL + 20\log_{10}(\beta). \tag{7}$$

Reynolds number effects were neglected. The frequency correction ensures that the Mach numbers are identical in the rig as in the scaled fan, i. e. the rotational fan speed needs to decrease inversely to the increased, scaled diameter. The amplitude correction accounts for the fact that acoustic power is an extensive quantity that needs to be scaled with the cross-sectional area of the nacelle. Since acoustic pressure is an intensive property and thus unaffected by any scaling, no further correction is required.

Funding Sources

This project has received funding from the Clean Sky 2 Joint Undertaking under the European Union's Horizon 2020 research and innovation program under grant agreement No 681856 - ASPIRE.

The presented ACAT1 data were obtained in the frame of the project TurboNoiseBB, which has received funding from the European Union's Horizon 2020 research and innovation program under grant agreement No. 690714.

Acknowledgments

The authors acknowledge Attila Wohlbrandt for helping to initiate this work. Furthermore, the authors thank Roland Ewert, Jürgen Dierke, and Nils Reiche (DLR) for their continued support and advice.

References

[1] Schnell, R., Goldhahn, E., and Julian, M., "Design and Performance of a Low Fan-Pressure-Ratio Propulsion System," *24th ISABE Conference*, Canberra, Australia, 2019.

[2] Moreau, A. and Guérin, S., "The impact of low-speed fan design on noise: an exploratory study," *Journal of Turbomachinery*, Vol. 138, No. 8, 2016, pp. 081006–1–13. doi:10.1115/1.4032678.

[3] Cumpsty, N. A., "Preparing for the future: reducing gas turbine environmental impact - IGTI scholar lecture," *Journal of Turbomachinery*, Vol. 132, No. 4, 2010, pp. 041017–1–17. doi:10.1115/1.4001221.

[4] Prasad, A. and Prasad, D., "Unsteady Aerodynamics and Aeroacoustics of a High-Bypass Ratio Fan Stage," *Journal of Turbomachinery*, Vol. 127, No. 1, Feb. 2005, pp. 64–75. doi:10.1115/1.1811103.

[5] Gill, J., Zhang, X., Joseph, P., and Nodé-Langlois, T., "Reduced dimension modeling of leading edge turbulent interaction noise," *20th AIAA/CEAS Aeroacoustics Conference*, Atlanta, Georgia, USA, 2014. doi:10.2514/6.2014-2321.

[6] Polacsek, C., Clair, V., Le Garrec, T., Reboul, G., and Jacob, M. C., "Numerical predictions of turbulence/cascade-interaction noise using computational aeroacoustics with a stochastic model," *AIAA Journal*, Vol. 53, No. 12, 2015, pp. 3551–3566. doi:10.2514/1.J053896.

[7] Reboul, G., Cader, A., Polacsek, C., Le Garrec, T., Barrier, R., and Nasr, N. B., "CAA Prediction of Rotor-Stator Interaction Using Synthetic Turbulence: Application to a Low-Noise Serrated OGV," *23rd AIAA/CEAS Aeroacoustics Conference*, Denver, Colorado, USA, 2017. doi:10.2514/6.2017-3714.

[8] Kim, J. W. and Haeri, S., "An advanced synthetic eddy method for the computation of aerofoil-turbulence interaction noise," *Journal of Computational Physics*, Vol. 287, 2015, pp. 1–17. doi: 10.1016/j.jcp.2015.01.039.

[9] Gea-Aguilera, F., Gill, J., Angland, D., and Zhang, X., "Wavy Leading Edge Airfoils Interacting with Anisotropic Turbulence," *23rd AIAA/CEAS Aeroacoustics Conference*, Denver, Colorado, USA, 2017. doi:10.2514/6.2017-3370.

[10] Wohlbrandt, A., Kissner, C., and Guérin, S., "Impact of cyclostationarity on fan broadband noise prediction," *Journal of Sound and Vibration*, Vol. 420, April 2018, pp. 142–164. doi:10.1016/j.jsv.2018.01.039.

[11] Gea-Aguilera, F., Gill, J., and Zhang, X., "On the effects of fan wake modelling and vane design on cascade noise," *Journal of Sound and Vibration*, Vol. 459, 2019. doi:10.1016/j.jsv.2019.114859.

[12] Ewert, R., Dierke, J., Siebert, J., Neifeld, A., Appel, C., Siefert, M., and Kornow, O., "CAA broadband noise prediction for aeroacoustic design," *Journal of Sound and Vibration*, Vol. 330, No. 17, 2011, pp. 4139–4160. doi:10.1016/j.jsv.2011.04.014.

[13] Siefert, M. and Ewert, R., "Sweeping Sound Generation in Jets Realized with a Random Particle-Mesh Method," *15th AIAA/CEAS Aeroacoustics Conference*, Miami, Florida, USA, 2009. doi:10.2514/6.2009-3369.

[14] Wohlbrandt, A., Hu, N., Guérin, S., and Ewert, R., "Analytical reconstruction of isotropic turbulence spectra based on the Gaussian transform," *Computers and Fluids*, Vol. 132, 2016, pp. 46–50. doi: 10.1016/j.compfluid.2016.03.023.

[15] Ewert, R., Dierke, J., Neifeld, A., and Moghadam, S. A., "Linear-and Non-Linear Perturbation Equations with Relaxation Source Terms for Forced Eddy Simulation of Aeroacoustic Sound Generation," *20th AIAA/CEAS Aeroacoustics Conference*, Atlanta, Georgia, USA, 2014. doi:10.2514/6.2014-3053.

[16] Delfs, J. W., Bauer, M., Ewert, R., Grogger, H., Lummer, M., and Lauke, T., "Numerical Simulation of Aerodynamic Noise with DLR's aeroacoustic code PIANO," Tech. rep., German Aerospace Center (DLR), Braunschweig, Germany, 2008.

[17] Hu, F. Q., Hussaini, M. Y., and Manthey, J. L., "Low-dissipation and low-dispersion Runge - Kutta schemes for computational acoustics," *Journal of Computational Physics*, Vol. 124, No. 1, 1996, pp. 177–191. doi:10.1006/jcph.1996.0052.

[18] Tam, C. K. and Webb, J. C., "Dispersion-relation-preserving finite difference schemes for computational acoustics," *Journal of Computational Physics*, Vol. 107, No. 2, 1993, pp. 262–281. doi: 10.1006/jcph.1993.1142.

[19] Kissner, C. A., Wohlbrandt, A. M., and Guérin, S., "Enhanced Fan Broadband Noise Prediction Based on a 2D Synthetic Turbulence Method," *24th AIAA/CEAS Aeroacoustics Conference*, Atlanta, Georgia, USA, 2018. doi:10.2514/6.2018-3452.

[20] Becker, K., Heitkamp, K., and Kügeler, E., "Recent Progress in a Hybrid Grid CFD Solver for Turbomachinery Flows," *Proc. V European Conference on Computational Fluid Dynamics ECCOMAS CFD 2010*, Lisbon, Portugal, 2010.

[21] Cécora, R.-D., Radespiel, R., Eisfeld, B., and Probst, A., "Differential Reynolds-stress modeling for aeronautics," *AIAA Journal*, Vol. 53, No. 3, 2015, pp. 739–755. doi:10.2514/1.J053250.

[22] Guérin, S. and Holewa, A., "Fan tonal noise from aircraft aeroengines with short intake: A study at approach," *International Journal of Aeroacoustics*, Vol. 17, No. 6-8, 2018, pp. 600–623. doi: 10.1177/1475472X18789001.

[23] Kissner, C. A., Guérin, S., and Behn, M., "Assessment of a 2D Synthetic Turbulence Method for Predicting the ACAT1 Fan's Broadband Noise," *25th AIAA/CEAS Aeroacoustics Conference*, Delft, The Netherlands, 2019. doi:10.2514/6.2019-2501.

[24] De Roeck, W., Desmet, W., Baelmans, M., and Sas, P., "An overview of high-order finite difference schemes for computational aeroacoustics," *Proceedings of the International Conference on Noise and Vibration Engineering*, Citeseer, 2004, pp. 353–368.

[25] Guérin, S., Kissner, C., Kajasa, B., Jaron, R., Behn, M., Hakansson, S., Pardowitz, B., Tapken, U., Meyer, R., and Enghardt, L., "Trends in fan broadband noise of the ACAT1 fan," 25th AIAA/CEAS Aeroacoustics Conference, Delft, Netherlands, 2019.

[26] Tapken, U., Pardowitz, B., and Behn, M., "Radial mode analyis of fan broadband noise," 23rd AIAA/CEAS Aeroacoustics Conference, Denver, Colorado, USA, 2017.

[27] Behn, M., Pardowitz, B., and Tapken, U., "Separation of tonal and broadband noise components by cyclostationary analysis of the modal sound field in a low-speed fan test rig," Fan2018, Darmstadt, Germany, 2018.

[28] Nallasamy, M. and Envia, E., "Computation of rotor wake turbulence noise," *Journal of Sound and Vibration*, Vol. 282, No. 3-5, April 2005, pp. 649–678. doi:10.1016/j.jsv.2004.03.062.

[29] Envia, E. and Coupland, J., "Panel Session - Fan Broadband Noise Prediction," *21st AIAA/CEAS Aeroacoustics Conference*, Dallas, Texas, USA, 2015. doi:10.2514/6.2014-3053.